View metadata, citation and simi
provided by

Role of Ag in Textured-annealed $Bi_2Ca_2Co_{1.7}O_x$ Thermoelectric Ceramic

D. Flahaut[a]*, J. Allouche[a], A. Sotelo[b], Sh. Rasekh[b], M. A. Torres[b], M. A. Madre[b], J. C. Diez[b]

[a]IPREM, Université de Pau, Hélioparc Pau Pyrénées, 2 av. Pierre Angot, 64053 Pau cedex 9, France

[b]Instituto de Ciencia de Materiales de Aragón, ICMA (CSIC-Universidad de Zaragoza), Mª de Luna, 3. 50018 Zaragoza, Spain

Andrés Sotelo Mieg	asotelo@unizar.es
Joachim Allouche	joachim.allouche@univ-pau.fr
Delphine Flahaut	delphine.flahaut@univ-pau.fr
Shahed Rasekh	shrasekh@unizar.es
Mª Antonieta Madre Sediles	amadre@unizar.es
Juan Carlos Díez Moñux	monux@unizar.es
Miguel Angel Torres Portero	matorres@unizar.es

Corresponding Author

* Delphine Flahaut +33 5 40 17 50 06

IPREM-ECP, Université de Pau, Hélioparc Pau Pyrénées, 2 av. Pierre Angot, 64053 Pau cedex 9, France

delphine.flahaut@univ-pau.fr

ABSTRACT: $Bi_2Ca_2Co_{1.7}O_x$ thermoelectric ceramics with small Ag additions (0, 1, 2, 3, 4, and 5 wt.%) have been successfully grown from the melt, using the laser floating zone method and subsequently annealed at 800 ºC for 24 h. The microstructure has shown a reduction of the amount of secondary phases for Ag contents up to 4 wt.%. This microstructural evolution leads to a decrease of the electrical resistivity values until an Ag content of 4 wt.%, whereas Seebeck coefficient has been maintained unchanged. This is in agreement with the presence of metallic Ag in all samples, confirmed not only by Energy Dispersive Spectrometry but also by X-ray photoelectron and Auger spectroscopy. These electrical properties lead to maximum power factor values of about 0.30 $mW/K^2.m$ at 650 ºC for the 4 wt.% Ag containing samples, which is among the best results obtained for this type of materials.

KEYWORDS: Texture, Thermoelectric materials, misfit, X-ray Photoelectron Spectroscopy (XPS), Auger Electron Spectroscopy (AES)

1. INTRODUCTION

Thermoelectric (TE) materials are able to transform thermal to electrical energy due to the well-known Seebeck effect, without moving parts. Nowadays, the energy transforming systems are characterized by their low efficiency and more than 50% of the energy consumption is wasted as heat. In this scenario, the TE energy conversion can provide very important advantages to harvest wasted heat in a wide number of applications, increasing their efficiency. At the same time, it could decrease the CO_2 emissions, helping to fight against global warming. Moreover, it can produce green energy transforming solar energy into electricity at lower cost than photovoltaic conversion [1]. The conversion efficiency of such materials is quantified by the dimensionless figure of merit ZT, which is defined as $TS^2/\rho\kappa$, where T, S, ρ, and κ are the absolute temperature, Seebeck coefficient, electrical resistivity, and thermal conductivity, respectively [2]. On the other hand, the electrical part of the expression (S^2/ρ) is called power factor, PF, and it is generally used for TE materials characterization, mostly when it is difficult to measure thermal conductivity. Moreover, it has been shown that efficiency is as important as the output power density, and this last parameter is proportional to the PF of TE material [3]. As a consequence, as stated by W. Liu *et al.*, the best approach for the improvement of TE materials is to increase PF and then optimize the physical design parameters [3].

Now, TE materials are used in a wide range of applications such as refrigeration, wasted heat harvesting in automobile exhausts, or in radioisotope thermoelectric generators (RTG) [4,5]. Most of these TE devices are based on either alloys or intermetallic thermoelectric materials, such as Bi_2Te_3 or $CoSb_3$, for which the thermoelectric performances are high at relatively low temperatures. On the other hand, these materials can be either oxidized or degraded at high temperatures under air, releasing toxic or heavy elements. As a consequence, their applications range is limited to relatively low temperatures.

This limitation in working temperatures was overtaken by the discovery of large thermoelectric properties in Na_xCoO_2 [6]. Following this discovery, great efforts have been made in the study of CoO-based materials, such as Ca-Co-O, Bi-Sr-Co-O, or Bi-Ca-Co-O, with attractive thermoelectric properties [7-12]. The crystal structure of these materials is composed by an alternate stacking of two different layers, a common conductive CdI_2-type CoO_2 layer with a two-dimensional triangular lattice and a block one, composed of insulating rock-salt-type (RS) ones. The two sublattices (RS block and CdI_2-type CoO_2 layer) possess common a- and c-axis lattice parameters and β angles but different b-axis lengths, causing a misfit along the b-direction [13].

As layered cobaltites are materials possessing a strong crystallographic anisotropy, they tend to crystallize in form of stacked plate-like grains leading to highly anisotropic microstructure and properties. As a consequence, the alignment of these plate-like grains along a preferential direction is necessary to reach properties comparable with those obtained on single crystals. Some established and well-known techniques are useful to obtain a good grain orientation in various oxide ceramic systems, such as template grain growth (TTG) [14], hot-pressing [15], spark plasma sintering [16], or directional growth from the melt with or without applied electrical current [17,18].

On the other hand, some works have shown that metallic Ag additions are useful to improve mechanical and electrical properties in several electroceramic systems [19,20]. At present, in the best of our knowledge, very few articles are dealing with Ag additions in Bi-AE-Co-O system (AE= alkaline earth) [21-23], while many more have been performed in the $Ca_3Co_4O_9$ system [24-26]. In all these studies, the role of Ag has not been clearly determined and some works report on Ag addition [24] while others consider Ag doping [25].

Taking into account these previously discussed effects, the aim of this work is to produce high performances TE materials by adding metallic Ag to the Bi-Ca-Co-O compound and establish the Ag role in the composite. The samples used in this work were directionally grown by a texturing process performed by the Laser Floating Zone (LFZ) technique, followed by annealing at 800 ºC for 24 h under air.

2. EXPERIMENTAL SECTION

The initial $Bi_2Ca_2Co_{1.7}O_x$-x wt.% Ag (x = 0, 1, 2, 3, 4, and 5) polycrystalline ceramics were prepared from commercial $Bi(NO_3)_3 \bullet 5H_2O$ ($\geq$ 98%, Aldrich), $CaCO_3$ ($\geq$ 99%, Panreac), $Co(NO_3)_2 \bullet 6H_2O$ (98 % Panreac), and metallic Ag (99%, Aldrich) compounds by a sol-gel method via nitrates [27]. The powders were weighed in the appropriate proportions and dissolved in a mixture of HNO_3 (analysis grade, Panreac) and distilled water. To the clear pink solution, citric acid (99.5%, Panreac), and ethylene glycol (99%, Panreac), were added in the adequate proportions. Evaporation of the solvent was slowly performed to decompose the nitric acid excess. Thus, the polymerization reaction between ethylene glycol and citric acid may occur and produce coordination compounds containing all the cations in a pink gel form [28]. Once dried, the product is heated at 350-400 ºC until its decomposition by slow self-combustion. The remaining powder was mechanically ground and calcined at 750 and 800 °C for 12 h, with an intermediate grinding. This step is of special importance when texturing is performed from the melt using the LFZ technique: it has been used to assure the alkaline-earth carbonates decomposition which, otherwise, would decompose in the molten zone disturbing the solidification front and producing grain misorientation. The so-obtained powders were isostatically cold-pressed in form of cylinders (~ 120 mm in length and 2-3 mm in diameter) under an applied pressure of about 200 Mpa for 1 min.

The green ceramic cylinders were subsequently used as feed in a LFZ texturing system successfully employed in previous works [29]. All samples were grown at the same rate (30 mm/h), with 3 rpm seed rotation, to maintain the cylindrical geometry in the final textured material. Simultaneously, the feed has been rotating at 15 rpm, in the opposite direction, to improve the compositional homogeneity of the molten zone. After the texturing process, long (more than 150 mm) cylindrical and geometrically homogeneous samples have been obtained. These textured materials were then cut into shorter pieces with the appropriate lengths for their characterization (~ 15 mm long). Finally, the samples were annealed at 800 ºC for 24 h under air after the solidification process. This thermal treatment is necessary to promote the formation of the thermoelectric phase due to the fact that the Bi-Ca-Co-O system presents incongruent melting and, during the solidification process, high amount of secondary phases is produced [22].

The structural identification of all the samples has been made through powder XRD utilizing a Rigaku D/max-B X-ray powder diffractometer (Cu Kα radiation) with 2θ ranging between 10 and 60 degrees. Microstructural observations have been performed on polished samples using a Field Emission Scanning Electron Microscope (FESEM, Carl Zeiss Merlin) fitted with energy dispersive spectrometry (EDS) analysis. Moreover, apparent density was measured using Archimedes' principle for each composition, at least for four ceramic samples, and compared to the theoretical density of each composition using 6.35 g/cm^3 for the $Bi_2Ca_2Co_{1.7}O_x$ phase [28], and 10.5 g/cm^3 for Ag [30].

The Auger analyses were carried out with a JEOL JAMP 9500F Auger spectrometer (JEOL Ltd, Tokyo, Japan) working under UHV conditions (pressure < 2.10^{-7} Pa). The UHV equipment is a Schottky field emission Auger electron spectrometer (FE-AES) dedicated to very high spatial resolution analysis and high brightness. The hemispherical electron analyzer coupled with a multichannel detector (7 channeltrons) offered ideal settings for energy resolved Auger analysis. The material cross-cut sections were prepared with a JEOL Cross-Polisher (JEOL Ltd, Tokyo, Japan). The cylinders were pasted on a silicon wafer before being preliminary cut with a diamond saw to obtain a first rough surface. The materials were then exposed in the Cross-polisher to a Ar^+

ion beam (working pressure of 1 x 10^{-4} Pa; ion beam energy varying from 1 to 6 keV; ion current, approximately, 120 μA) before being mounted on the Auger sample holder.

The X-ray photoelectron spectroscopy (XPS) analyses were made in a Thermo K-alpha system with a hemispherical analyzer and a microfocused (analysis area was ca. 200 μm^2) monochromatized radiation Al Kα line (1486.6 eV) operating at 75 W under a residual pressure of 1 x 10^{-9} mbar in order to characterize the surface atomic composition and chemical environment of elements at surface of all samples. The spectrometer pass energy was set to 200 eV for survey spectrum and to 20 eV for core peak records. Surface charging was minimized using a neutralizer gun which sprays low energy electrons and Ar^+ ions over the sample surface. All the binding energies were referenced to the C 1s peak at 285.0 eV which is originated from surface carbon contamination. The treatment of core peaks was carried out using a nonlinear Shirley-type background. A weighted least-squares fitting method, using 70% Gaussian and 30% Lorentzian line shapes, was applied to optimize the peak positions and areas. The quantification of surface composition was based on Scofield's relative sensitivity factors [31].

Steady-state simultaneous measurements of resistivity and Seebeck coefficient were performed by the standard dc four-probe technique in a LSR-3 apparatus (Linseis GmbH) between 50 and 650 ºC under He atmosphere. From these data, PF values as a function of temperature were calculated to evaluate the final samples TE performances.

3. RESULTS AND DISCUSSION

Powder XRD patterns for all $Bi_2Ca_2Co_{1.7}O_x$ samples with different Ag content are plotted in Fig. 1 together with their Rietveld pattern matching performed with FullProf [32] using the $Bi_2Ca_2Co_{1.7}O_x$ (C2/m space group #12) and Ag ($Fm\bar{3}m$ space group #225) cells. As it can be observed in the figure, all the samples show very similar patterns and the most intense peaks correspond to the misfit cobaltite $Bi_2Ca_2Co_{1.7}O_x$ phase, in agreement with previously reported data [33]. From these patterns, it can be deduced that the performed thermal treatment has been effective to produce nearly single cobaltite phase, independently of Ag content. On the other hand, metallic Ag has also been identified in the Ag containing samples. When considering the fitting results, shown in the graph, some evident differences between the calculated and the observed diffraction patterns can be observed. These differences are mainly due to two factors: 1) peaks appearing at around 19 and 29 degrees cannot be taken into account due to the fact that there are not enough diffraction peaks to determine the phase at which they belong. Probably they correspond to a remaining secondary phase. 2) As it is well known, the thermoelectric phase is characterized by an intrinsic aperiodicity in the structure while the space group used for the Rietveld pattern matching does not possess this aperiodicity. In order to estimate the accuracy of these fittings, the profile factor (R_p), weighted profile factor (R_{wp}), and Bragg factor (R_B) have been obtained following the procedure reported in [32] and summarized in Table I.

Table I: R_p, R_{wp}, and R_B agreement factors calculated with FullProf for all the $Bi_2Ca_2Co_{1.7}O_x$ samples with different metallic Ag additions.

wt.% Ag	**0**	**1**	**2**	**3**	**4**	**5**
R_p	21.4	16.0	16.9	16.6	15.8	15.4
R_{wp}	29.4	23.0	23.9	25.0	23.3	25.2
R_B	2.6	2.4	2.0	2.2	2.2	2.0

On the other hand, when observing the figure it is clear that, at least, some part of Ag is kept as metallic one, in agreement with previously reported data in similar systems [34,35]. On the other hand, it could be considered that some part of Ag might be inserted in the crystal structure [25,36] due to the similar ionic radii of Ag^+, Bi^{3+}, and Ca^{2+}. In order to check if some Ag is substituting these cations in the RS layer, cell parameters have also been determined from the Rietveld refinement and the results are displayed in Table II.

As reported in the table, no significant differences can be found in the cell parameters and the differences in the calculated cell volumes are too small to be significant. As a result, it can be deduced that no structural changes are produced by the different Ag additions, indicating that Ag does not seem to be incorporated in the crystal structure. Consequently, it can be expected that metallic Ag could be found finely dispersed all along the samples in agreement with previous works [19,20,37,38].

Scanning electron microscopy has been performed on polished longitudinal sections of all samples. The microstructural evolution of samples, as a function of Ag content, can be easily observed in Fig. 2, where representative micrographs of all samples are presented. In these general views, four contrasts can be distinguished, each one associated to a different phase through EDS with a lateral resolution of 1 μm (spot diameter 2 μm) and numbered, for clarity, in Figs. 3a and c. Grey contrast (#1) corresponds to the thermoelectric $Bi_2Ca_2Co_{1.7}O_x$ phase, white (#2) and black (#3) ones to the Bi_3CaO_y and CoO secondary phases, respectively, and light grey (#4) to metallic Ag. From the micrographs, it appears that CoO secondary phase is considerably reduced when silver is added. Moreover, the amount of the Bi_3CaO_y phase is also reduced for Ag contents up to 4 wt.%.

Table II: Cell parameters calculated with FullProf for all the $Bi_2Ca_2Co_{1.7}O_x$ samples with different metallic Ag additions.

wt.% Ag	a (Å)	b(Å)	c (Å)	β (°)
0	4.8857 (6)	5.1953 (9)	29.326 (1)	93.655 (9)
1	4.8653 (7)	5.1883 (9)	29.276 (1)	93.47 (1)
2	4.8899 (8)	5.1902 (9)	29.279 (1)	93.61 (1)
3	4.8927 (8)	5.194 (1)	29.293 (1)	93.57 (1)
4	4.908 (1)	5.190 (1)	29.277 (2)	93.27 (1)
5	4.8865 (6)	5.186 (1)	29.331 (8)	93.648 (9)

Further Ag addition starts to raise the amount of this secondary phase. As a consequence of these microstructural modifications, the amount of TE $Bi_2Ca_2Co_{1.7}O_x$ phase is clearly maximum for the 4 wt.% Ag doped samples.

On the other hand, silver particles are not easy to observe in the micrographs displayed in Fig. 2 due to their small sizes. In order to observe the shape and distribution of the silver particles, higher magnification micrographs have been recorded for samples with 4 wt.% Ag, and presented in Fig. 3. In those micrographs, some Ag particles are indicated by arrows in the sake of clarity, as they show nearly the same contrast observed in the thermoelectric phase. Furthermore, these Ag particles show an elongated shape and appear between the thermoelectric grains, probably improving their electrical connectivity, as reported in previous works in similar textured systems [19,20], or in solid state sintered materials [39]. Moreover, Ag addition seems to slightly decrease porosity of samples, probably due to the formation of a eutectic phase, as it was already found in similar systems [38].

To confirm the previous SEM observations and characterize chemical order structure with higher spatial resolution, Auger Electron Spectroscopy (AES) nanoprobe analyses were performed on cross-cut sections of all samples. For 0 wt.% Ag (Fig. 4), a systematic surface chemical characterization was carried out on a representative material cross-cut section (upper left SEM image) by successively focusing the excitation beam (~ 6-10 nm in diameter) on three target zones, corresponding to the thermoelectric $Bi_2Ca_2Co_{1.7}O_x$ (dot no.1), Bi_3CaO_y (dot no.2) and CoO (dot no.3) phases. In good agreement with the previous SEM observations, the Auger spectra on upper right of Fig. 4 exhibits Bi NVV (80-120 eV), Ca LMM (240-320 eV), Co LMM (618-775) and O KLL (468-505 eV) transitions for the dot no.1 [40].

On the other hand, the spectrum of the dot no.2 displays only Bi, Ca and O transitions with no Co detection. Finally, analysis of dot no.3 shows only Co and O transition with a lack of Ca and Bi signals. Moreover, we can identify the C KLL (240-280 eV) transition, which can probably occur for the dots no.1 and no.2. For these latter ones, this transition cannot clearly be observed probably due to the Ca LMM and C KLL transitions signals overlapping in this energy window. To better appreciate the location of the different Bi, Ca and Co rich domains, AES chemical mapping was carried out on the whole cross-cut section to enhance chemical contrast (lower part of Fig. 4). Bi (red), Ca (green) and Co (blue) individual maps have been recorded and compiled in a Bi-Ca-Co overlay. In such overlay, the Bi (red) and Co (blue) rich domains corresponding to the secondary Bi_3CaO_y and CoO phases, respectively, are clearly identifiable. Such phases are dispersed between the grains of the thermoelectric $Bi_2Ca_2Co_{1.7}O_x$ phase (cyan color) which combines the presence of the all Bi, Ca and Co elements. Chemical mapping of O was not represented for a better clarity.

For materials with 4 wt.% Ag, the same conditions of analysis were applied (Fig. 5) but, taking into account the Ag presence, an additional target dot (dot no.4) is provided on SEM cross-cut section image corresponding to the analysis of an Ag domain. As it can be seen, the spectra of thermoelectric and secondary phases (dots no.1, 2 and 3) are identical to those obtained for 0 wt.% Ag material. On the spectrum of dot no.4, we can clearly observe the Ag MNN (260-356 eV) transition and the absence all other Bi, Ca, Co and O elements. Such results confirm the presence of silver as small metallic inclusions in the thermoelectric phase instead of its incorporation in the crystal structure. In addition, AES chemical maps have been provided for Bi (red), Ca (green), Co (blue), Ag (magenta) and O (yellow). As it can be seen on the Bi-Ca-Co-Ag overlay map, Ag inclusions are clearly identifiable among all other Bi, Ca and Co rich domains. We can also notice the size reduction of the Bi_3CaO_y (deep red and white domains in overlay and SEM image, respectively) and CoO (deep blue and black domains in overlay and SEM image, respectively) phases.

Such results complete the previous SEM and EDS analyses highlighting the benefit of a high spatial resolution (≈ 6 nm) chemical mapping for the characterization of such materials when several multiphase domains coexist at nano- or micrometer scale. Indeed, Auger spectroscopy could provide an elemental chemical composition signature of TE materials spatially resolved at nano-scale enhancing the identification of domains and their precise location.

To more precisely investigate the chemical environments and oxidation states of the elements in the as-prepared samples, XPS analyses of all samples have been performed. The Bi 4f, Ca 2p, Co 2p, O 1s, C 1s and Ag 3d core peaks have been recorded and compositions from those analyses have been established. The Ca 2p, O 1s and C 1s core peaks are not shown here for clarity. The corresponding binding energies (B.E.) and atomic percentages are reported in Table III. The Ag content is very low and remains almost constant in all materials. Consequently, the evolution of Ag content in the series of compounds cannot be conclusive but may be regarded as a trend. The O 1s core peaks can be decomposed into three components at 528.8, 529.1 and 530.9 eV according to Ca-O, M-O (M = Co and Bi) and adsorbed species environments. The Ca 2p spectra consists in two peaks (Ca $2p_{3/2}$ and Ca $2p_{1/2}$) separated by 3.5 eV. Each peak can be decomposed into two components, the major one is assigned to calcium in CaO environment (B.E. (Ca $2p_{3/2}$) = 345.6 eV) and the second one to $CaCO_3$ (B.E. (Ca $2p_{3/2}$) = 347.0 eV). The C 1s signal is associated to the carbon contamination always observed in XPS, mainly when alkaline or alkaline earths are present due to their tendency to form carbonates. As a consequence, the C 1s component at 289.3 eV can be correlated to the formation of $CaCO_3$ formed after atmospheric exposure of the samples.

The Bi 4f core peaks of the $Bi_2Ca_2Co_{1.7}O_x$ – x Ag series are shown in Fig. 6. Due to the spin-orbit coupling, each spectrum is composed of two peaks (Bi $4f_{7/2}$ and Bi $4f_{5/2}$) separated by 5.4 eV. As expected, the intensity ratio I(Bi $4f_{7/2}$)/I(Bi $4f_{5/2}$) is close to 1.3.

The Bi $4f_{7/2}$ component of the non-doped sample is located at 158.5 eV. This value is assigned to bismuth in an oxygenated octahedron in the Bi^{3+} oxidation state [41,42]. The Ag doping does not affect the global shape of the Bi 4f core peaks. Nonetheless, we can notice a small shift at lower binding energy (B.E. (Bi $4f_{7/2}$) = 154.3 eV) after Ag doping for all compositions.

The Co 2p core peaks are represented in Fig. 7. The spectra are split into two parts (Co $2p_{3/2}$ and Co $2p_{1/2}$) due to the spin-orbit coupling, with an intensity ratio close to 2/1. Each part consists of a main line and a satellite peak. The Co $2p_{3/2}$ and the Co $2p_{1/2}$ components exhibit main lines at 779.0 eV and 789.1 eV with satellite peaks at 794 eV and 804.5 eV, respectively. The presence of a main line together with a satellite peak (shake-up) results from a ligand-to-metal charge transfer during the photoemission process. As no satellite peak is observed at 6 eV at high B.E. side of the main peaks (characteristic of Co^{2+}), we can conclude that the cobalt is trivalent in the misfit phase.

When the misfit phase is doped with silver, the overall shape of the Co 2p core peak is retained. But, if we take a closer look of the area ratio between the satellite and main peak, a very slight evolution of the I_{sat}/I_{main} value can be put in evidence. In the literature, Dahéron et al. [43] reported that the evolution of the cobalt oxidation state from +3 towards +4 could be discriminated by considering the broadening of the main peak towards higher binding energies and the decrease of the satellite peak relative area. From the value of I_{sat}/I_{main}, it can be deduced that the 4% Ag compound exhibits the highest content of Co^{4+} (~ 3%).

On Fig. 8, the Ag 3d spectra are presented. Even if they are relatively noisy, the B.E. of the Ag $3d_{5/2}$ component at 367.8 eV allows to conclude that Ag is in metallic state, which is consistent with the Auger spectroscopy observations.

The temperature dependence of the electrical resistivity, together with its corresponding error (~4 %), as a function of Ag content is presented in Fig. 9. The $\rho(T)$ curve of

Ag-free samples exhibits a semiconducting-like behaviour ($d\rho/dT < 0$) from room temperature (RT) to about 500 ºC and a metallic-like one ($d\rho/dT > 0$) at higher temperatures. Addition of silver to the samples involves a change in the electrical behaviour. For the samples containing 1 wt.% Ag, a semiconducting-like behaviour in the whole measured temperature range can be observed. However, larger Ag additions lead to a slightly metallic-like behaviour in all the samples. The increase of silver content up to 4 wt.% leads to a stepped decrease of resistivity values. Above this content, the electrical resistivity starts to rise. This evolution of the electrical resistivity is in agreement with the microstructural evolution shown in Fig. 3. The amount of TE phase is raised for Ag contents up to 4 wt.% and decreased for higher additions. This effect can be due to the possible formation of a "$Bi_2Ca_2Co_{1.7}O_x$"-Ag eutectic phase with an Ag content of about 4 wt.%, as it has been found in similar systems [38]. The presence of this eutectic could improve the grains connectivity reducing the electron scattering at grain boundaries, inducing a drop of the electrical resistivity. Thus, the minimum value of the resistivity at RT and 650 ºC is close to 25 mΩ.cm for both temperatures in samples containing 4 wt.% Ag. On the other hand, the Ag-free sample exhibits a value of about two times higher, ~ 49 and 47 mΩ.cm at RT and 650 ºC, respectively.

Table III: Binding energies (B.E. (eV) and atomic percentages (%) of BiCaCoO-x Ag samples with (x = 0, 1, 2, 3, 4 and 5)

	BiCaCoO		BiCaCoO 1% Ag		BiCaCoO 2 %Ag		BiCaCoO 3% Ag		BiCaCoO 4% Ag		BiCaCoO 5% Ag	
	B.E. (eV)	%	B.E. (eV)	%	B.E. (eV)	%	B.E. (eV)	%	B.E. (eV)	%	B.E. (eV)	%
Ag 3d$_{7/2}$			367.8	0.3	367.8	0.2	367.8	0.2	367.8	0.2	367.8	0.2
Bi 4f$_{7/2}$	158.5	15.4	158.5	15.8	158.3	11.2	158.5	15.8	158.3	16.4	158.1	16.5
Ca 2p$_{3/2}$	345.7	10.9	345.7	10.1	345.6	7.0	345.7	11.5	345.6	11.8	345.5	11.9
	347.3	1.2	347.1	1.9	346.6	1.9	347.1	1.2	346.8	2.2	347.0	1.4
		12.1		12.1		8.9		12.7		14.0		13.3

Co $2p_{3/2}$	779.0	5.6	779.0	5.9	779.0	3.9	779.0	6.2	779.0	7.2	779.0	6.5
O 1s	528.9	25.6	528.8	14.7	528.8	18.4	528.7	19.1	528.8	14.0	528.9	17.7
	530.8	14.6	529.0	13.1	529.9	6.4	529.1	9.1	529.1	17.4	529.2	13.2
			530.8	14.8	531.3	5.5	530.8	13.3	530.9	12.7	531.0	10.8
					533.1	1.9						
		40.2		42.6		32.2		41.4		44.1		41.7
C 1s	285.0	21.3	285.0	18.1	285.0	35.7	285.0	19.1	285.0	14.7	285.0	17.8
	286.6	2.0	286.6	1.6	286.3	4.3	286.5	1.1	286.5	0.9	286.9	1.1
	288.1	1.9	288.5	1.7	288.0	1.7	288.3	1.5	288.2	0.8	288.4	1.3
	289.3	1.7	289.4	2.0	289.2	2.2	289.5	1.7	289.3	1.7	289.5	1.7
		26.9		23.4		43.9		23.4		18.1		21.9

In any case, these values are lower than the ones obtained in Pb-doped $Bi_2Ca_2Co_{1.7}O_x$ processed by the LFZ technique (~ 33 mΩ.cm) [44] and bulk sintered materials (~ 100 mΩ.cm) [32] at RT. On the other hand, it is still high compared with the obtained in Ag-free $Bi_2Ca_2Co_2O_x$ single crystals [12], or solid state sintered samples with different Ag additions (~ 15 mΩ.cm) [39]. This result clearly indicates that further improvements of these bulk materials, from the point of view of their texture and electrical connectivity between the grains, can be produced by using lower growth rates [45].

Fig. 10 displays the variation of the Seebeck coefficient, together with its corresponding error (~4 %), as a function of temperature for all samples. First, the positive values presented for the Seebeck coefficient in the whole measured temperature range, confirm that the conduction mechanism is predominantly governed by holes. Moreover, a nearly linear increase of the Seebeck values with temperature can be observed. This trend could be associated with a typical behavior of a metal or degenerated semiconductor when the variation of carrier concentration, effective mass, and Fermi level with temperature can be considered negligible. Furthermore, all the samples exhibit, approximately, the same Seebeck coefficient values independently of the Ag content. The Seebeck coefficient values at RT and 650 ºC values (~ 160 and 280 μV/K, respectively) are higher than the measured in $Bi_2Ca_2Co_2O_x$ single crystals without Ag (about 130 and 170 μV/K, respectively) [12]. Nonetheless, they are close to the values reported for classically sintered materials at RT (~ 155 μV/K) [32]. The origin of such high Seebeck coefficient values is the formation of a significant amount of oxygen vacancies in the thermoelectric phase when the samples are textured by using the LFZ technique [29]. Moreover, these vacancies are not totally filled during the annealing procedure due to the low porosity found in these samples (see Figure 3) which hinders the oxygen diffusion into the inner part of the samples. This fact has been checked by apparent density measurements which showed values of 5.97, 6.05, 6.10, 6.13, 6.17, and 6.23 g/cm^3 for samples with 0, 1, 2, 3, 4, and 5 wt.% Ag, confirming the observations previously discussed in the SEM section. These measured densities correspond to 94.0, 94.9, 95.3, 95.4, 95.6, and 96.2 % of the theoretical ones calculated from the mixture of Ag and $Bi_2Ca_2Co_{1.7}O_x$ phases. These results are in agreement with previously published results in other similar TE systems [46]. Furthermore, it has also been observed in the misfit phase $[Ca_2CoO_3][CoO_2]_{1.62}$ which contains considerable amounts of oxygen vacancies when the samples are thermally treated under a reducing atmosphere [47,48]. The rise of the oxygen vacancies changes the Co oxidation state from Co^{4+} to Co^{3+}, which makes increasing the S values, in agreement with the Koshibae equation [49].

In order to evaluate the thermoelectric performances of the textured ceramic materials, the PF has been calculated from the resistivity and Seebeck coefficient values. The obtained values at different temperatures are presented, as a function of the Ag content, in Fig. 11. Moreover, the corresponding errors were calculated by error transmission, leading to values of around 10 %. Consistently with the resistivity measurements, PF values at RT increase with Ag contents until reaching a maximum for the 4 wt.% Ag samples. Further Ag addition induces a decrease of PF values. The maximum values obtained at RT and 650 ºC (~ 0.11 and 0.30 mW/K^2.m, respectively) are much higher than those obtained in the Ag-free materials prepared in this work (around 0.05 and 0.18 mW/K^2.m, respectively). Furthermore, they are much higher than those measured on sintered materials at RT (~ 0.02 mW/K^2.m) [33]. On the other hand, they are still lower than those obtained in $Bi_2Ca_2Co_2O_x$ single crystals (about 0.26 and 0.41 mW/K^2.m at RT and 650 ºC, respectively) [12], clearly indicating that further improvements are still possible. All these results indicate that adding a small Ag content is a good way to strongly reduce the electrical resistivity and, consequently, improve the thermoelectric performances of textured $Bi_2Ca_2Co_{1.7}O_x$ ceramics.

4. CONCLUSIONS

This paper demonstrates that $Bi_2Ca_2Co_{1.7}O_x$ thermoelectric materials with small Ag additions (0, 1, 2, 3, 4, and 5 wt.%) can be directionally grown by the laser floating zone method. It has been determined that the optimal Ag content in the textured materials after annealing is 4 wt.%. Microstructural evolution shows that this amount of Ag significantly reduces the proportion of secondary phases. Moreover, XPS and Auger spectra have confirmed that Ag is maintained in the metallic state in all cases. Furthermore, in agreement with the microstructure evolution, the electrical resistivity data clearly indicated that 4 wt.% Ag addition produces an important reduction of the materials resistivity. All these factors lead to a rise in PF reaching a maximum value of ~ 0.30 mW/K^2.m at 650 ºC which is relatively close to the values obtained in single crystals and higher than those obtained in polycrystalline samples.

ACKNOWLEDGMENT

This research has been supported by the Spanish MINECO-FEDER (MAT2013-46505-C3-1-R). The authors wish to thank the Gobierno de Aragón-FEDER (Consolidated Research Groups T87 and T12) for financial support and to C. Gallego, and C. Estepa for their technical assistance. Authors would like to acknowledge the use of Servicio General de Apoyo a la Investigación-SAI, Universidad de Zaragoza.

REFERENCES

1. W. Liu, X. Yan, G. Chen, Z. Ren, Recent Advances in Thermoelectric Nanocomposites, Nano Energy 1 (2012) 42-56.

2. D. M. Rowe, in: D. M. Rowe (Ed.), Thermoelectrics Handbook: Macro to Nano, 1st. edn., CRC Press, Boca Raton, FI, 2006, 1-3.

3. W. Liu, Q. Jie, H. S. Kim, Z. Ren. Current progress and future challenges in thermoelectric power generation: From materials to devices. Acta Mater. 87 (2015) 357-376.

4. S. Sharma, V. K. Dwivedi, S. N. Pandit, A Review of Thermoelectric Devices for Cooling Applications, Int. J. Green Energy 11 (2012) 899-909.

5. M. H. Elsheikh, D. A. Shnawah, M. F. M. Sabri, S. B. M. Said, M. H. Hassan, M. B. A. Bashir, M. A. Mohamad, A Review on Thermoelectric Renewable Energy: Principle Parameters that Affect their Performance, Renewable Sustainable Energy Rev. 30 (2014) 337-355.

6. I. Terasaki, Y. Sasago, K. Uchinokura, Large Thermoelectric Power in $NaCo_2O_4$ Single Crystals, Phys. Rev. B 56 (1997) 12685–12687.

7. R. Funahashi, I. Matsubara, H. Ikuta, T. Takeuchi, U. Mizutani, S. Sodeoka, An Oxide Single Crystal with High Thermoelectric Performance in Air, Jpn. J. Appl. Phys. 39 (2000) L1127–L1129.

8. V. Hardy, D. Flahaut, R. Fresard, A. Maignan, A. Anisotropic Susceptibility of the Geometrically Frustrated Spin-chain Compound $Ca_3Co_2O_6$, J. Phys.: Condens. Matter 19 (2007) 145229.

9. H. Leligny, D. Grebille, O. Perez, A. C. Masset, M. Hervieu, B. Raveau, A Five-dimensional Structural Investigation of the Misfit Layer Compound $[Bi_{0.87}SrO_2]_2[CoO_2]_{1.82}$, Acta Crystallogr., Sect. B: Struct. Sci. 56 (2000) 173–182.

10. W. Kobayashi, S. Hebert, H. Muguerra, D. Grebille, D. Pelloquin, A. Maignan, Thermoelectric Properties in the Misfit-layered-cobalt Oxides $[Bi_2A_2O_4]$ $[CoO_2]_{b1/b2}$ (A = Ca, Sr, Ba, b(1)/b(2)=1.65, 1.82, 1.98) Single Crystals, In I. Kim (Ed.), Proceedings ICT 07: Twenty-sixth international conference on thermoelectrics, Korea, 2008; pp. 117-120.

11. K. Rubesova, T. Hlasek, V. Jakes, S. Huber, J. Hejtmanek, D. Sedmidubsky, Effect of a Powder Compaction Process on the Thermoelectric Properties of $Bi_2Sr_2Co_{1.8}O_x$ Ceramics. J. Eur. Ceram. Soc. 35 (2015) 525-531.

12. N. Sun, S. T. Dong, B. B. Zhang, Y. B. Chen, J. Zhou, S. T. Zhang, Z. B. Gu, S. H. Yao, Y. F. Chen, Intrinsically Modified Thermoelectric Performance of Alkaline-earth Isovalently Substituted $[Bi_2AE_2O_4][CoO_2]_y$ Single Crystals, J. Appl. Phys. 114 (2013) 043705.

13. A. Maignan, S. Hebert, M. Hervieu, C. Michel, D. Pelloquin, D. Khomskii, Magnetoresistance and Magnetothermopower Properties of Bi/Ca/Co/O and Bi(Pb)/Ca/Co/O Misfit Layer Cobaltites, J. Phys.: Condens. Matter 15 (2003) 2711–2723.

14. H. Itahara, C. Xia, J. Sugiyama, T. Tani, Fabrication of Textured Thermoelectric Layered Cobaltites with Various Rock salt-type Layers by using b-$Co(OH)_2$ Platelets as Reactive Templates, J. Mater. Chem. 14 (2004) 61–66.

15. H. Wang, X. Sun, X. Yan, D. Huo, X. Li, J. G. Li, X. D. Ding, J. Fabrication and Thermoelectric Properties of Highly Textured $Ca_9Co_{12}O_{28}$ Ceramic, J. Alloys Compd. 582 (2014) 294-298.

16. N. Y. Wu, T. C. Holgate, N. V. Nong, N. Pryds, S. Linderoth, High Temperature Thermoelectric Properties of $Ca_3Co_4O_{9+\delta}$ by Auto-combustion Synthesis and Spark Plasma Sintering, J. Eur. Ceram. Soc. 34 (2014) 925-931.

17. J. C. Diez, Sh. Rasekh, M. A. Madre, E. Guilmeau, S. Marinel, A. Sotelo, Improved Thermoelectric Properties of Bi-M-Co-O (M = Sr, Ca) Misfit Compounds by Laser Directional Solidification, J. Electron. Mater. 39 (2010) 1601-1605.

18. N. M. Ferreira, Sh. Rasekh, F. Costa, M. A. Madre, A. Sotelo, J. C. Diez, M. A. Torres, New Method to Improve the Grain Alignment and Performance of Thermoelectric Ceramics, Mater. Lett. 83 (2012) 144-147.

19. A. Sotelo, M. A. Torres, G. Constantinescu, Sh. Rasekh, J. C. Diez, M. A. Madre, Effect of Ag Addition on the Mechanical and Thermoelectric Performances of Annealed $Bi_2Sr_2Co_{1.8}O_x$ Textured Ceramics, J. Eur. Ceram. Soc. 32 (2012) 3745-3751.

20. M. Mora, A. Sotelo, H. Amaveda, M. A. Madre, J. C. Diez, L. A. Angurel, G. F. de la Fuente, Ag Addition Effect on Laser Textured Bi-2212 Samples, Bol. Soc. Esp. Ceram. V. 44 (2005) 199-203.

21. R. Ang, Y. P. Sun, X. Luo, W. H. Song. A narrow band contribution with Anderson localization in Ag-doped layered cobaltites $Bi_2Ba_3Co_2O_y$. J. Appl. Phys. 102 (2007) 073721.

22. A. Sotelo, Sh. Rasekh, G. Constantinescu, M. A. Torres, M. A. Madre, J. C. Diez, Improvement of Textured $Bi_{1.6}Pb_{0.4}Sr_2Co_{1.8}O_x$ Thermoelectric Performances by Metallic Ag Additions, Ceram. Int. 39 (2013) 1597-1602.

23. S. Wang, Z. Bai, H. Wang, Q. Lu, J. Wang, G. Fu. High temperature thermoelectric properties of $Bi_2Sr_2Co_2O_y$/Ag composites. J. Alloys Compd. 554 (2013) 254-257.

24. P.-H. Xiang, Y. Kinemuchi, H. Kaga, K. Watari. Fabrication and thermoelectric properties of $Ca_3Co_4O_9$/Ag composites. J. Alloys Compd. 454 (2008) 364-369.

25. Y. Wang, Y. Sui, J. Cheng, X. Wang, J. Miao, Z. Liu, Z. Qian, W. Su. High temperature transport and thermoelectric properties of Ag-substituted $Ca_3Co_4O_{9+\delta}$ system. J. Alloys Compd. 448 (2008) 1-5.

26. Y. Wang, Y. Sui, J. Cheng, X. Wang, W. Su. Comparison of the high temperature thermoelectric properties for Ag-doped and Ag-added $Ca_3Co_4O_9$. J. Alloys Compd. 477 (2009) 817-821.

27. Sh. Rasekh, M. A. Madre, A. Sotelo, E. Guilmeau, S. Marinel, J. C. Diez. Effect of synthetic methods on the thermoelectrical properties of textured $Bi_2Ca_2Co_{1.7}O_x$ ceramics. Bol. Soc. Esp. Ceram. V. 49 (2010) 89-94.

28. A. Sotelo, Sh. Rasekh, M. A. Madre, E. Guilmeau, S. Marinel, J. C. Diez, Solution-based Synthesis Routes to Thermoelectric $Bi_2Ca_2Co_{1.7}O_x$, J. Eur. Ceram. Soc. 31 (2011) 1763-1769.

29. A. Sotelo, E. Guilmeau, M. A. Madre, S. Marinel, S. Lemmonier, J. C. Diez, $Bi_2Ca_2Co_{1.7}O_x$ Thermoelectric Ceramics Textured by Laser Floating Zone Method, Bol. Soc. Esp. Ceram. Vidrio 47 (2008) 225-228.

30. C. R. Hammond, in C. R. Hammond (Ed.), CRC Handbook of chemistry and physics, 90th edn. CRC Press, Boca Raton, Fl, 2006, 4-44−4-101

31. J. H. Scofield, Hartree-Slater Subshell Photoionization Cross-sections at 1254 and 1487 eV, J. Electron Spectrosc. Relat. Phenom. 8 (1976) 129−137.

32. J. Rodriguez-Carvajal, "FULLPROF: A Program for Rietveld Refinement and Pattern Matching Analysis", Abstracts of the Satellite Meeting on Powder Diffraction of the XV Congress of the IUCr, Toulouse, France (1990) p. 127.

33. E. Guilmeau, M. Pollet, D. Grebille, D. Chateigner, B. Vertruyen, R. Cloots, R. Funahashi, B. Ouladiaff, Neutron Diffraction Texture Analysis and Thermoelectric Properties of BiCaCoO Misfit Compounds, Mater. Res. Bull. 43 (2008) 394–400.

34. M. Mikami, N. Ando, R. Funahashi. The effect of Ag addition on electrical properties of the thermoelectric compound $Ca_3Co_4O_9$. J. Solid State Chem. 178 (2005) 2186-2190.

35. J. C. Diez, Sh. Rasekh, G. Constantinescu, M. A. Torres, M. A. Madre, A. Sotelo. Effect of Ag additions on the $Bi_{1.6}Pb_{0.4}Sr_2Co_{1.8}O_x$ thermoelectric properties. Bol. Soc. Esp. Ceram. V. 52 (2013) 93-97.

36. F. P. Zhang, Q. M. Lu, J. X. Zhang, X. Zhang. Texture and high temperature transport properties of $Ag_xCa_{3-x}Co_4O_9$ ($0 \leq x \leq 0.6$) compounds. J. Alloys Compd. 477 (2009) 543-546.

37. N. V. Nong, A. J. Samson, N. Pryds, S. Linderoth, Microstructure and Thermoelectric Properties of Screen-Printed Thick Films of Misfit-Layered Cobalt Oxides with Ag Addition. J. Electron. Mater. 41 (2012) 1280-1285.

38. P. Majewski, A. Sotelo, H. Szillat, S. Kaesche, F. Aldinger, Phase Diagram Studies in the System Ag-"$Bi_2Sr_2CaCu_2O_8$", Physica C 275 (1997) 47-51.

39. B. Rivas-Murias, H. Muguerra, M. Traianidis, C. Henrist, B. Vertruyen, R. Cloots. Enhancement of the power factor of $[Bi_{1.68}Ca_2O_4]^{RS}[CoO_2]_{1.69}$ - Ag composites prepared by the spray-drying method. Solid State Sci. 12 (2010) 1490-1495.

40. D. C. Kenton, B. A. Carlson, L. A. LaVanier, C. L. Hedberg, Handbook of Auger Electron Spectroscopy: a Book of Reference Data for Identification and Interpretation in Auger Electron Spectroscopy Third Edition, 1995, Physical Electronics Industries.

41. T. P. Nguyen, E. Faulques, P. Molinier, XPS Studies of the Bi-Sr-Ca-Cu-O Ceramics at Temperatures near T, Phys. Rev. B 48 (1993) 12989-12992.

42. X. Xue, G. Tan, W. Liu, H. Ren, Structural, Electrical and Magnetic Properties of $(Bi_{0.9}RE_{0.1})(Fe_{0.97}Co_{0.03})O_3$ (RE=Nd and Gd) Thin Films, Mater. Res. Bull.52 (2014) 143-150.

43. L. Dahéron, R. Dedryvère, H. Martinez, M. Ménétrier, C. Denage, C. Delmas, D. Gonbeau, Electron Transfer Mechanisms upon Lithium Deintercalation from $LiCoO_2$ to CoO_2 investigated by XPS, Chem. Mater. 20 (2008) 583-590.

44. A. Sotelo, E. Guilmeau, Sh. Rasekh, M. A. Madre, S. Marinel, J. C. Diez, Enhancement of the Thermoelectric Properties of Directionally Grown Bi-Ca-Co-O through Pb for Bi Substitution, J. Eur. Ceram. Soc. 30 (2010) 1815-1820.

45. Sh. Rasekh, G. Constantinescu, M. A. Torres, M. A. Madre, J. C. Diez, A. Sotelo. Growth rate effect on microstructure and thermoelectric properties of melt grown $Bi_2Ba_2Co_2O_x$ textured ceramics. Adv. Appl. Ceram. 111 (2012) 490-494.

46. M. A. Madre, F. M. Costa, N. M. Ferreira, A. Sotelo, M. A. Torres, G. Constantinescu, Sh. Rasekh, J. C. Diez, Preparation of High-performance $Ca_3Co_4O_9$ Thermoelectric Ceramics produced by a New Two-step Method, J. Eur. Ceram. Soc. 33 (2013) 1747-1754.

47. M. Karppinen, H. Fjellvåg, T. Konno, Y. Morita, T. Motohashi, H. Yamauchi, Evidence for Oxygen Vacancies in Misfit-Layered Calcium Cobalt Oxide, $[CoCa_2O_3]_qCoO_2$, Chem. Mater. 16 (2004) 2790-2793.

48. D. Moser, L. Karbonen, S. Populoh, M. Trottman, A. Weidenkaff, Influence of the Oxygen Content on Thermoelectric Properties of $Ca_{3-x}Bi_xCo_4O_{9+\delta}$ System, Solid State Sci. 13 (2011) 2160-2164.

49. W. Koshibae, K. Tsutsui, S. Maekawa, Thermopower in Cobalt Oxides, Phys. Rev. B 62 (2000) 6869-6872.

Figure 1. Observed, calculated, and difference between the observed and calculated diffraction patterns from the Rietveld refinement of XRD data of $Bi_2Ca_2Co_{1.7}O_x$ samples with different Ag contents: a) 0; b) 1; c) 2; d) 3; e) 4; and f) 5 wt.%. The vertical green lines indicate the allowed reflection positions of $Bi_2Ca_2Co_{1.7}O_x$ and Ag phases. The inserts show a zoom on the region of (111) Ag diffraction plane.

Figure 2. Scanning electron micrographs from longitudinal polished textured samples $Bi_2Ca_2Co_{1.7}O_x$ with different Ag contents: a) 0; b) 1; c) 2; d) 3; e) 4; and f) 5 wt.%. The different contrasts are shown by numbers and associated through EDS to different phases: 1) grey, $Bi_2Ca_2Co_{1.7}O_x$; 2) white, Bi_3CaO_y; 3) black, CoO; and 4) light grey, Ag.

Figure 3. Scanning electron micrograph obtained in a representative longitudinal polished sample $Bi_2Ca_2Co_{1.7}O_x$ with 4 wt.% Ag. Some Ag particles are indicated by arrows.

Figure 4. Auger Electron Spectroscopy Analyses of 0 wt.% Ag cross-cut section material with cross-cut section SEM image (upper right), Auger spectra of three target dots (upper left) and Bi, Ca, Co and Bi-Ca-Co overlay Auger chemical maps (lower part). Scale bar = 10 μm.

Figure 5. Auger Electron Spectroscopy Analyses of 4 wt.% Ag cross-cut section material with cross-cut section SEM image (upper right), Auger spectra of four target dots (upper left) and Bi, Ca, Co, Ag, Bi-Ca-Co-Ag overlay and O Auger chemical maps (lower part). Scale bar = 10 μm.

Figure 6. Bi 4f core peaks of BiCaCoO-x Ag samples with (x = a) 0; b) 1; c) 2; d) 3; e) 4; and f) 5 wt.%).

Figure 7. Co 2p core peaks of BiCaCoO-x Ag samples with (x = a) 0; b) 1; c) 2; d) 3; e) 4; and f) 5 wt.%).

Figure 8. Ag 3d core peaks of BiCaCoO-x Ag samples with(x = a) 1; b) 2; c) 3; d) 4; and e) 5 wt.%).

Figure 9. Temperature dependence of the electrical resistivity, with its corresponding error, for textured $Bi_2Ca_2Co_{1.7}O_x$ with different Ag content.

Figure 10. Temperature dependence of the Seebeck coefficient, with its corresponding error, for textured $Bi_2Ca_2Co_{1.7}O_x$ with different Ag content.

Figure 11. Temperature dependence of the power factor, with its corresponding error, for textured $Bi_2Ca_2Co_{1.7}O_x$ with different Ag content.

Figure 1

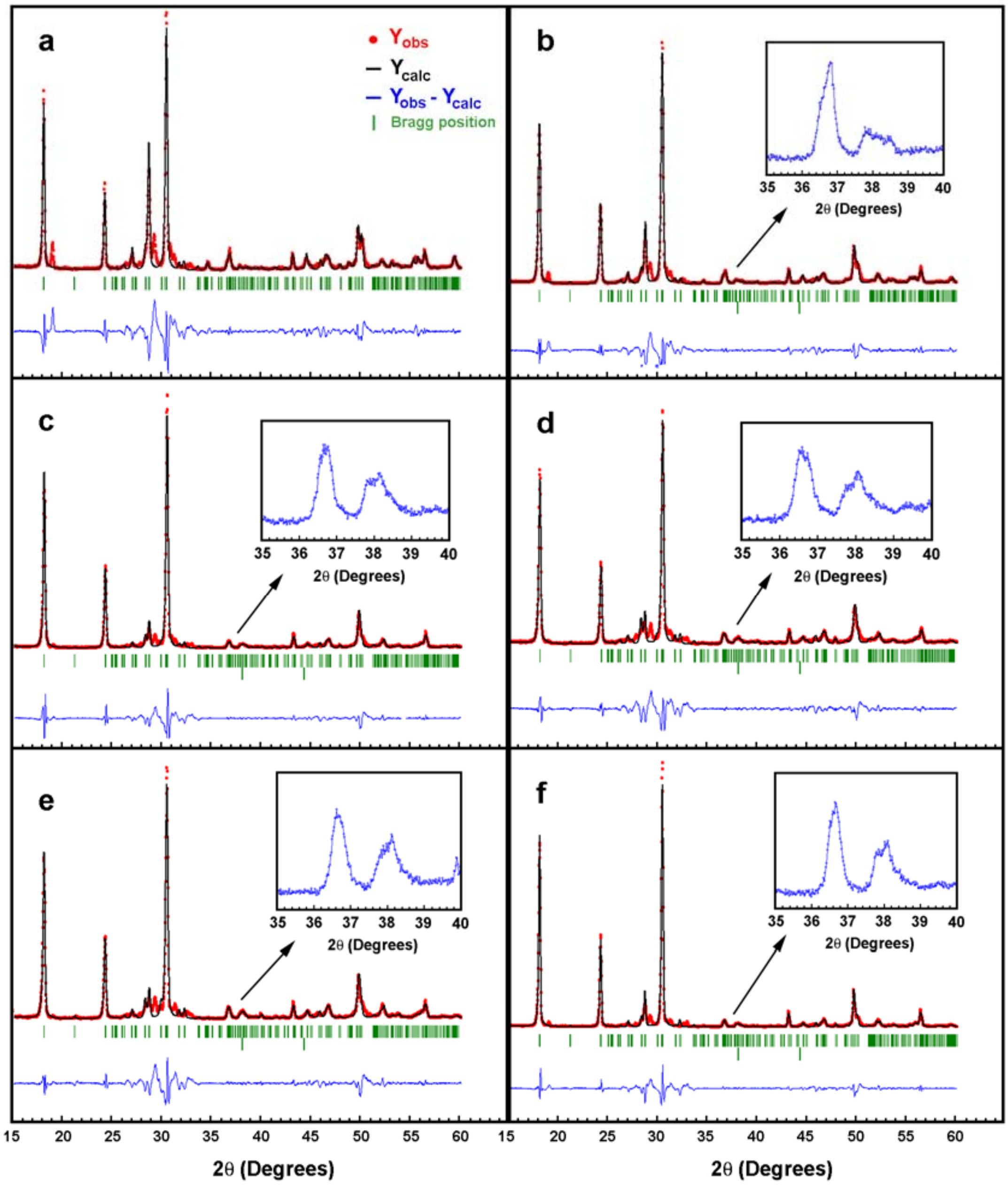
a
b
c
d
e
f
Y_obs
Y_calc
Y_obs - Y_calc
Bragg position
35 36 37 38 39 40
2θ (Degrees)
15 20 25 30 35 40 45 50 55 60
2θ (Degrees)
15 20 25 30 35 40 45 50 55 60
2θ (Degrees)

Figure 2

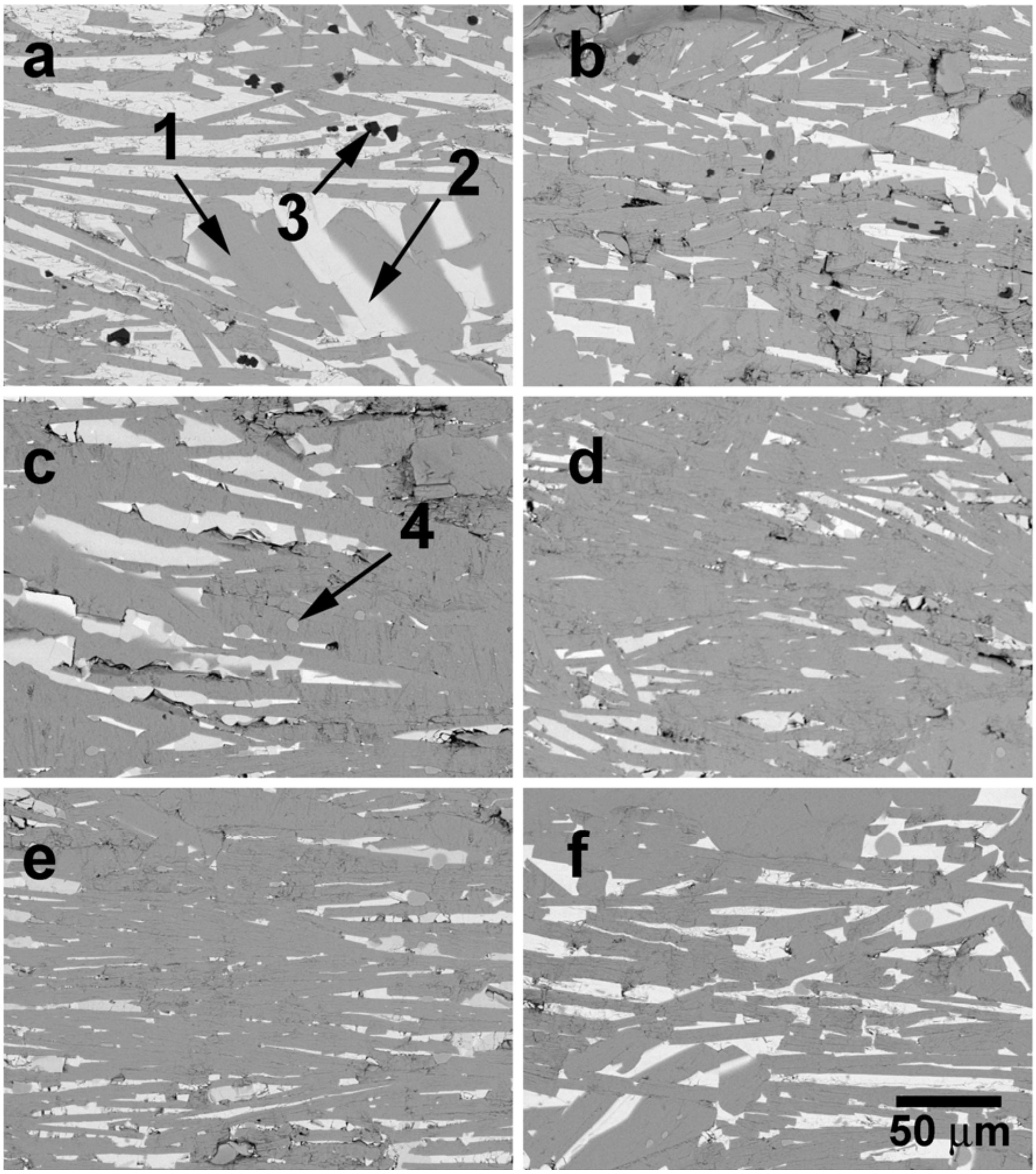

a
1
3
2
b
c
4
d
e
f
50 µm

Figure 3

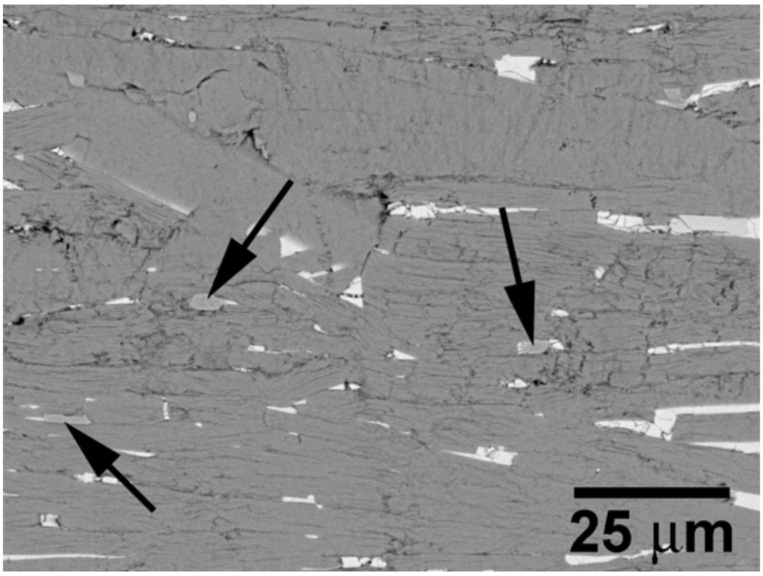

Figure 4

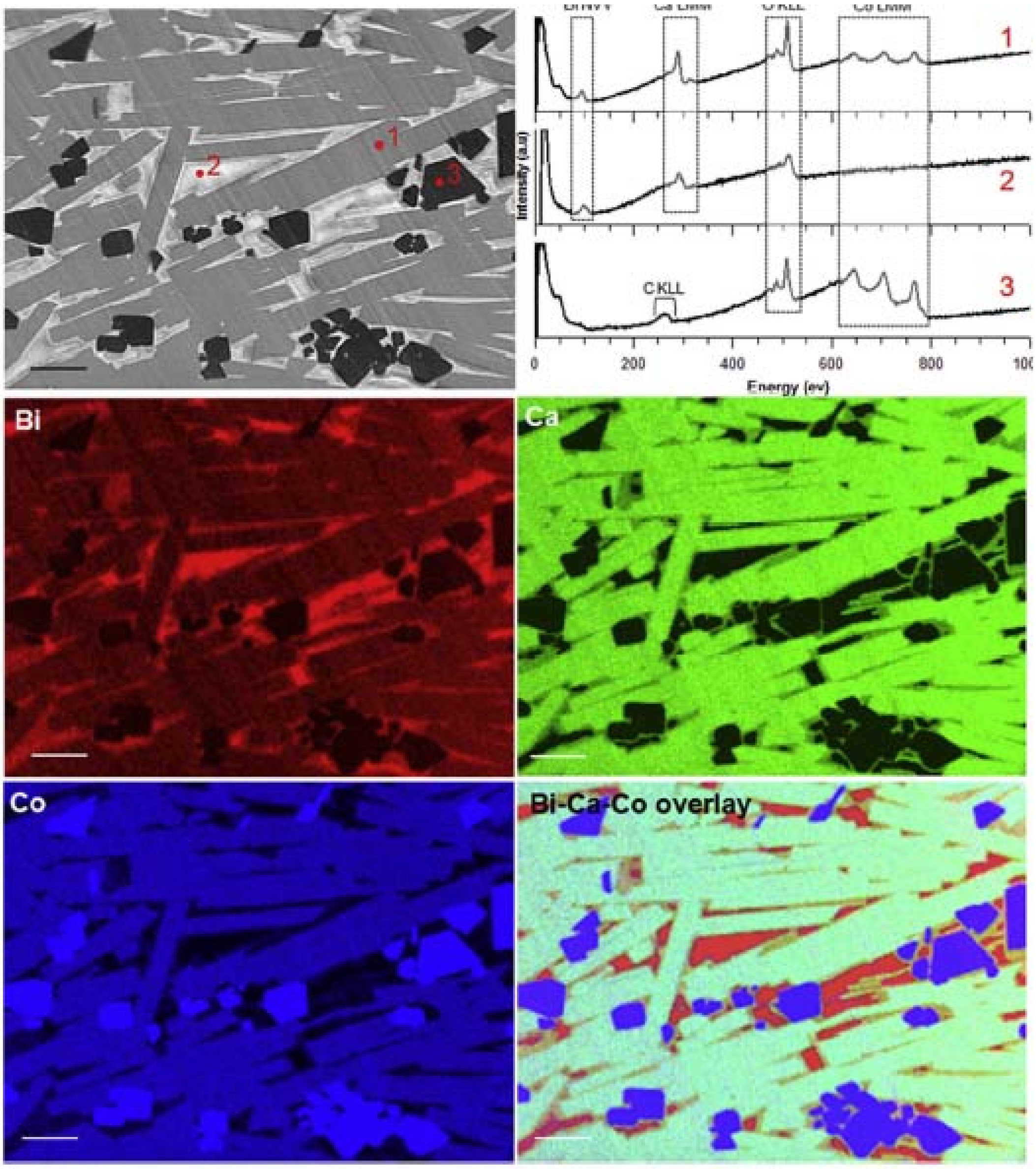
1
2
3
Bi NVV
Ca LMM
O KLL
Co LMM
C KLL
Intensity (a.u)
Energy (ev)
0
200
400
600
800
Bi
Ca
Co
Bi-Ca-Co overlay

Figure 5

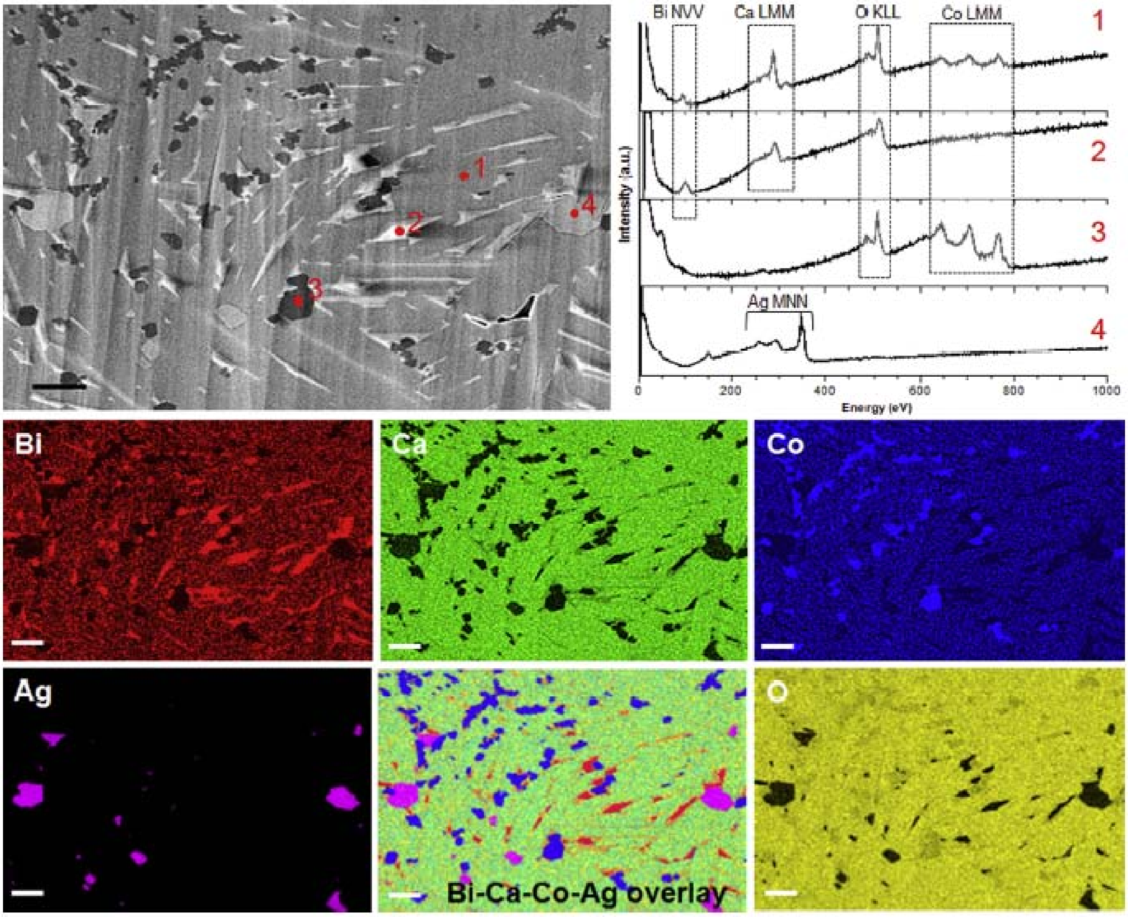
1
2
3
4
Bi NVV
Ca LMM
O KLL
Co LMM
Ag MNN
Intensity (a.u.)
Energy (eV)
0
200
400
600
800
1000
Bi
Ca
Co
Ag
Bi-Ca-Co-Ag overlay
O

Figure 6

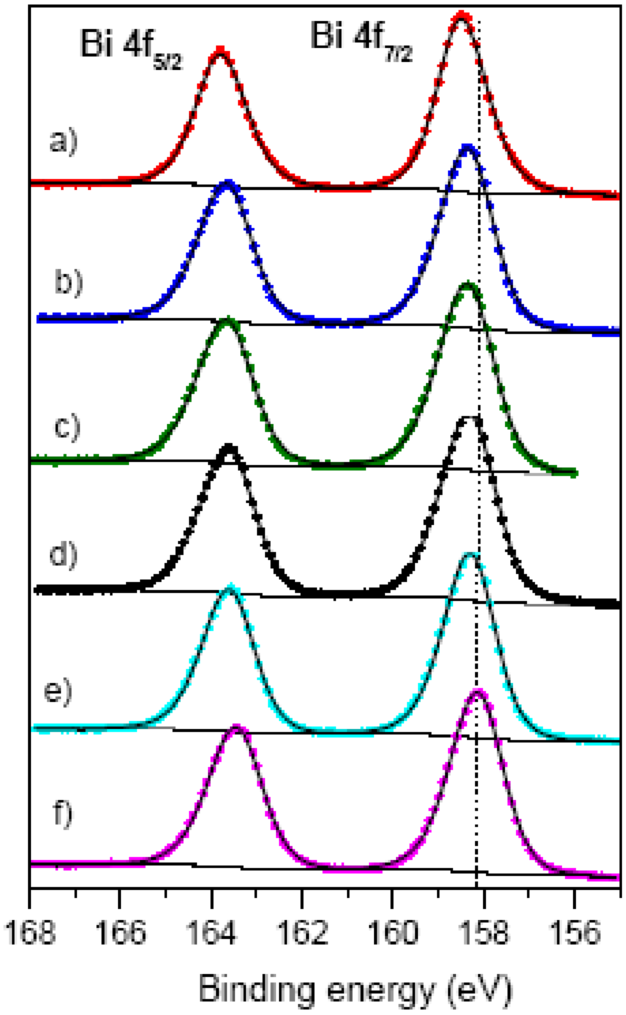
Bi 4f$_{5/2}$
Bi 4f$_{7/2}$
a)
b)
c)
d)
e)
f)
168
166
164
162
160
158
156
Binding energy (eV)

Figure 7

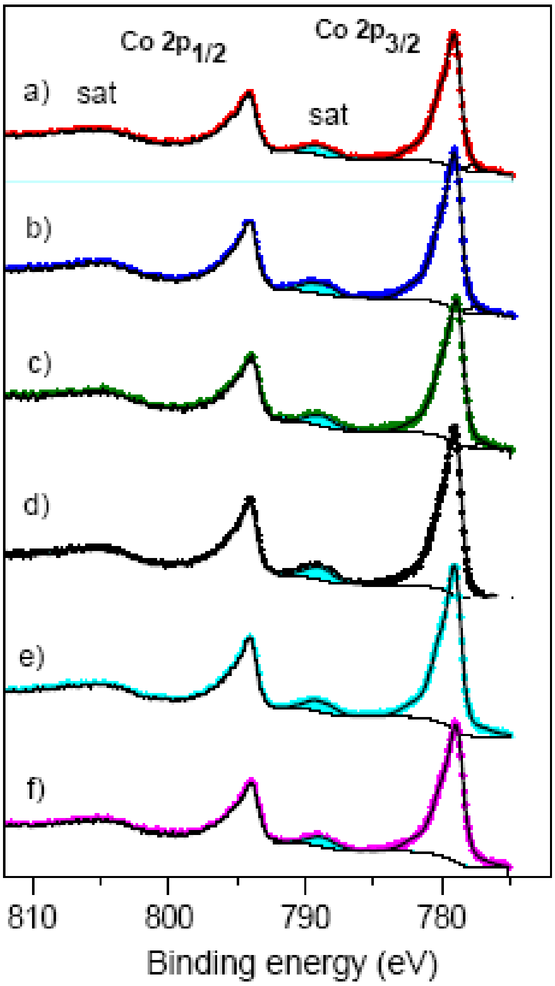
Co 2p$_{1/2}$
Co 2p$_{3/2}$
a)
sat
sat
b)
c)
d)
e)
f)
810
800
790
780
Binding energy (eV)

Figure 8

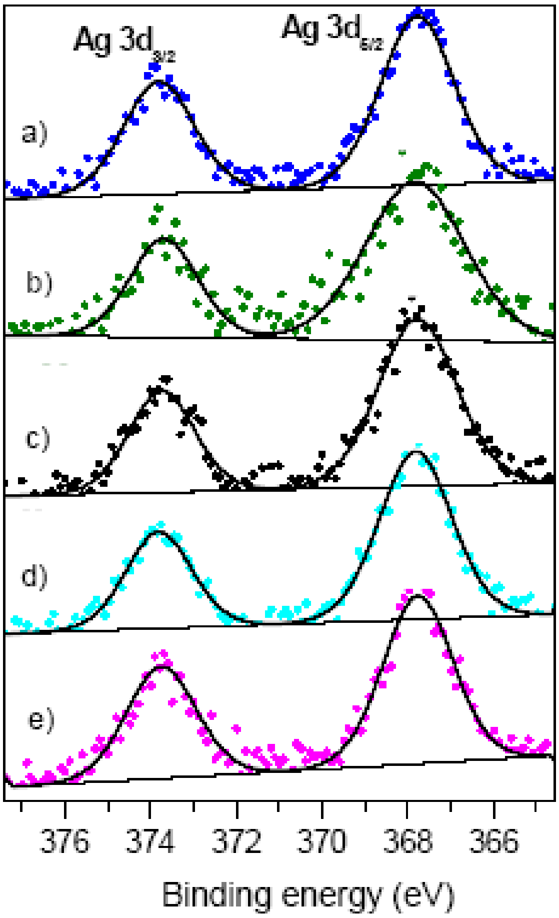
Ag 3d$_{3/2}$
Ag 3d$_{5/2}$
a)
b)
c)
d)
e)
376
374
372
370
368
366
Binding energy (eV)

Figure 9

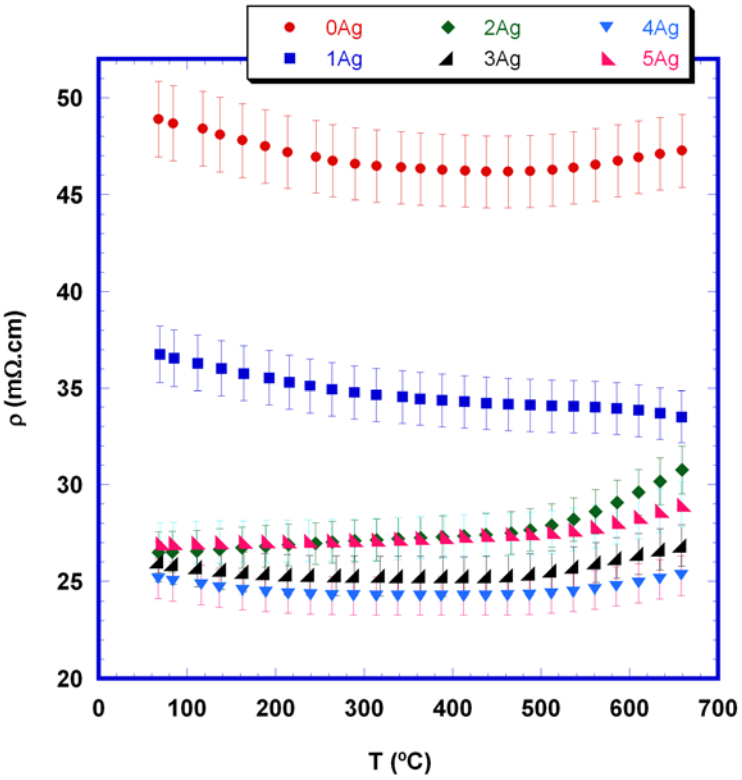
0Ag
2Ag
4Ag
1Ag
3Ag
5Ag
50
45
40
35
30
25
20
ρ (mΩ.cm)
0
100
200
300
400
500
600
700
T (ºC)

Figure 10

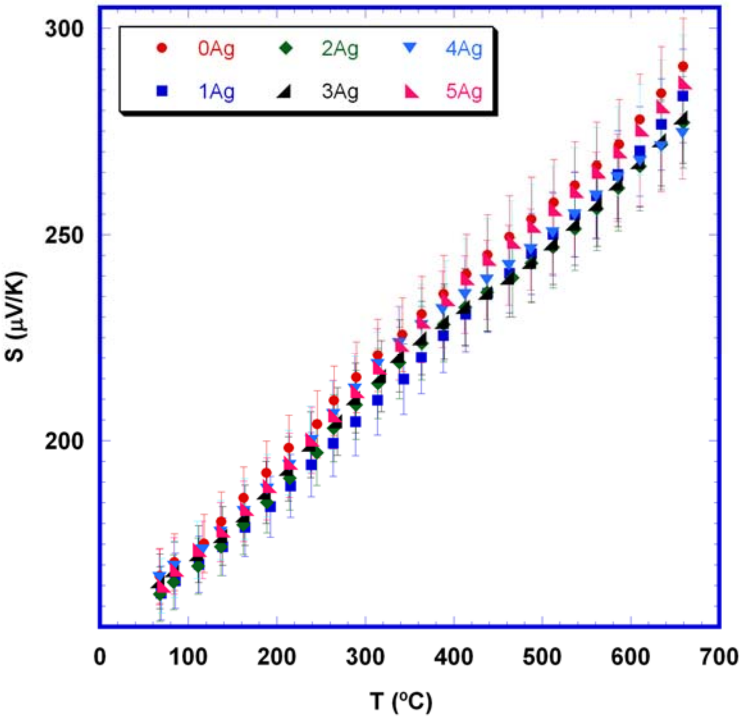
0Ag
2Ag
4Ag
1Ag
3Ag
5Ag
300
250
200
S (μV/K)
0
100
200
300
400
500
600
700
T (ºC)

Figure 11

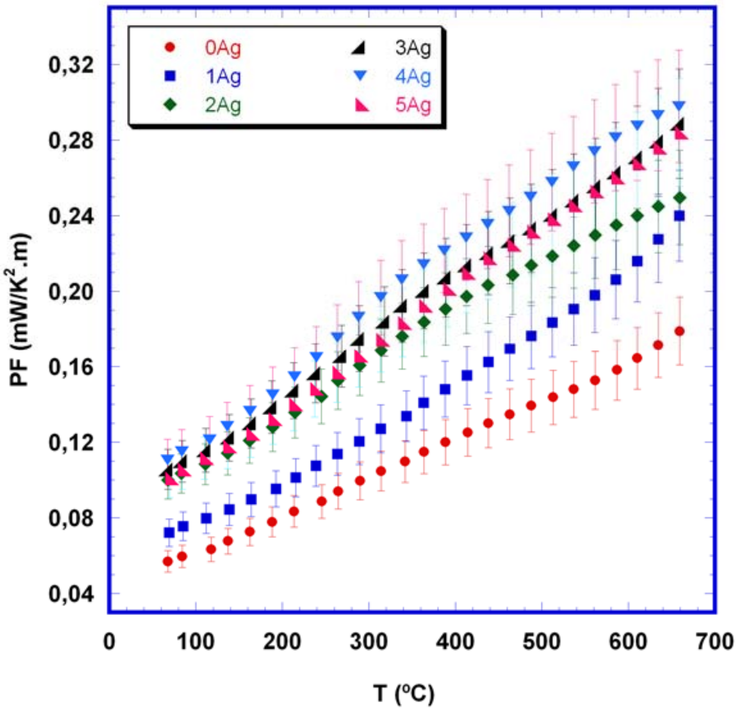
0Ag
1Ag
2Ag
3Ag
4Ag
5Ag
PF (mW/K^2.m)
0,04
0,08
0,12
0,16
0,20
0,24
0,28
0,32
0
100
200
300
400
500
600
700
T (ºC)